RESEARCH ARTICLE

Optimal Design of Single-Layer and Multi-Layer Air-Core Inductors Considering Uncertainty Factors

LU WAN[1], (Member, IEEE), **ARUN D. KHILNANI**[2], (Student Member, IEEE),
XINGLONG WU[3], (Member, IEEE), **XIAOKANG LIU**[3], (Senior Member, IEEE),
SERGIO A. PIGNARI[3], (Fellow, IEEE), **DAVID W. P. THOMAS**[2], (Senior Member, IEEE),
MARK SUMNER[2], (Senior Member, IEEE), **AND FLAVIA GRASSI**[3], (Senior Member, IEEE)

[1]Department of Energy, Aalborg University, 9220 Aalborg, Denmark
[2]Department of Electrical and Electronic Engineering, University of Nottingham, NG7 2RD Nottingham, U.K.
[3]Department of Electronics, Information and Bioengineering, Politecnico di Milano, 20133 Milan, Italy

Corresponding author: Flavia Grassi (flavia.grassi@polimi.it)

ABSTRACT Air-core inductors are key components in power converters and measurement equipment. To optimally design inductors, their self-resonant frequency (SRF) as a result of inherent stray capacitance should be accurately estimated. This paper presents optimal design procedures for air-core inductors, considering constraints such as SRF and inductor volume. To this end, a methodology is proposed to estimate the variability of stray capacitances, accounting for various uncertainty factors. Specifically, for single-layer air-core inductors, an empirical expression is adopted and experimentally verified to provide better predictions compared to the commonly used physical-based approach. For multi-layer air-core inductors, an enhanced analytical approach based on the energy-conservation method is proposed, which considers the impact of five influence factors. Two key factors (the proximity effect and the variation of turn length) are investigated by FEM simulations and incorporated into the enhanced models. The other three factors (the effective permittivity of the wire insulation coating, the winding tightness, and the electric field path assumption) are taken into account as uncertainty factors, leading to statistical estimates of the stray capacitance and SRF. Finally, two samples are fabricated for single- and multi-layer air-core inductors, which agree well with the design specifications, proving the effectiveness of the proposed design methodology.

INDEX TERMS Air-core inductor, optimal design, self-resonant frequency, stray capacitance.

I. INTRODUCTION

Air-core inductors are widely used in EMI filters [1], power electronic converters [2], and line impedance stabilization networks (LISNs) [3] with the advantage of avoiding hysteresis and eddy-current losses and holding large currents without saturation. However, because of their inherent capacitance (stray capacitance), the inductive behavior of air-core inductors is constrained up to the first self-resonant frequency (SRF), limiting the potential performance of designed applications at high frequency. Hence, in order to

The associate editor coordinating the review of this manuscript and approving it for publication was Norbert Herencsar.

design air-core inductors with inductive behavior within the frequency of interest, it is crucial to determine their stray capacitance.

This paper introduces a new design methodology for single-layer and multi-layer air-core inductors, which takes into account constraints defined by the SRF and the physical size (volume). To this end, several methods for predicting stray capacitance are analyzed and compared. In general, these techniques can be classified into three categories: finite element method (FEM) models, empirical formulas, and physical-based analytical models.

Although the FEM-based approach is time consuming, it is commonly used as a reference due to its precision [4]. Some

studies have focused on the accuracy of 2D and 3D models [5], while others have focused on improving the simulation efficiency [6].

The empirical expression is derived through a range of experiments or simulations conducted on different inductor samples with varied parameters. For instance, in [7], the derivation of a formula for the stray capacitance of coils by varying the coil diameter and length was introduced. Although it requires a substantial sample size for curve-fitting, the empirical expression can provide a rule of thumb for predictions.

According to physical-based approaches, the total equiv-alent stray capacitances of inductors mainly depend on the integration of electrostatic capacitances between adjacent conductor turns (i.e., turn-to-turn and layer-to-layer capac-itances). These basic static capacitances between adjacent turns can be determined based on the geometry and insulation material specifications of the conductors [8]. Two main approaches, based on different assumptions, are commonly employed to integrate basic static capaci-tances in order to determine the total stray capacitances: the lumped-capacitance network method and the energy-conservation method. The lumped-capacitance network is more suitable for single-layer inductors [9], as their equivalent circuits can be easily derived. Conversely, the energy-conservation method is preferable for multi-layer inductors and transformers [10]. The accuracies of these two approaches for a single-layer ferrite-core inductor were compared in [11], demonstrating that the energy-conservation method is more accurate. However, it is important to note that this conclusion may only be applicable to inductors with magnetic cores, and further validation is necessary for air-core inductors.

Therefore, regarding the single-layer air-core inductors, this work compares both physical-based approaches and empirical formulas through theoretical analyses and exper-imental tests, with the objective to derive a more precise methodology for estimating stray capacitances.

In terms of multi-layer air-core inductors, although the physical-based analytical approach provides more straight-forward procedures compared to the other two methods, it often leads to a large approximation of the observed stray capacitances from measurements [12]. One possible reason is that the analytical approaches ignore the geometry uncer-tainties and simplify the equations by assuming ideal winding conditions only. However, these geometry uncertainties have a significant impact on the derived equations and predictions. For instance, in [13], the proximity effect was considered, but the turn length variation across layers was ignored. The filling factors were proposed in [9] to account for winding tightness and fabrication process imperfections. The divergence in assumptions regarding the electric field further results in different stray capacitance predictions, as illustrated in [14] and [15]. Additionally, also the effective permittivity of the wire insulation coating, for which only an estimated interval of variation is usually known, [16], [17], has a non-negligible

influence on the prediction accuracy. Therefore, instead of predicting a specific stray-capacitance value based on an ideal winding geometry, it is more beneficial to provide an estimated range of variability, taking into account different uncertainty factors, including the influence of the proximity effect, the variation in turn length, the winding tightness, the electric field path assumption, and the effective permittivity of the wire insulation coating.

Therefore, in this work, an enhanced physical-based analytical modeling approach is introduced for multi-layer air-core inductors, which considers both orthogonal and hexagonal windings configurations. This approach accounts for proximity effects and variations in the turn length across layers, and their influence is verified using FEM simulation. Using the proposed modeling methods for the stray capacitances, new air-core inductor design procedures that consider uncertainties (such as the winding tightness in geometry, the electric field path assumption, and the effective permittivity of the wire insulation coating) are introduced through two real design examples.

The remaining sections of the paper are organized as follows. Section II compares different methods for pre-dicting stray capacitances in single-layer air-core inductors. The modeling approach for the design of multi-layer air-core inductors is proposed in Section III. The application example and the corresponding uncertainty analyses for single-layer and multi-layer air-core inductors are presented in Sections IV and V. Finally, conclusions are drawn in Section VI.

II. MODELING METHODS FOR SINGLE-LAYER INDUCTORS

This section provides a comparison of different approaches for predicting the stray capacitance of single-layer inductors. Particularly, the physical-based analytical approaches and methods based on empirical expressions are presented, and their accuracy is evaluated by comparing them with measurement results.

Physical-based analytical methods, which rely on geom-etry modeling, involve two steps for computing the total stray capacitance of an inductor. The first step computes the turn-to-turn capacitance (C_{tt}) between each loop turn of the inductor (refer to Section II-A). The second step aggregates these turn-to-turn capacitances to determine the total stray capacitance (C_{tot}) (see Section II-B). The lumped-capacitance network and the energy-conservation method are two commonly used approaches for the second step, each based on different assumptions.

A. TURN-TO-TURN CAPACITANCE
The capacitance between adjacent turns in air-core inductors is assumed to be equivalent to the capacitance between two parallel loop conductors with identical wire specifications. Specifically, this capacitance is computed by integrating the elementary capacitance of two circular conductors in 2D space [9].
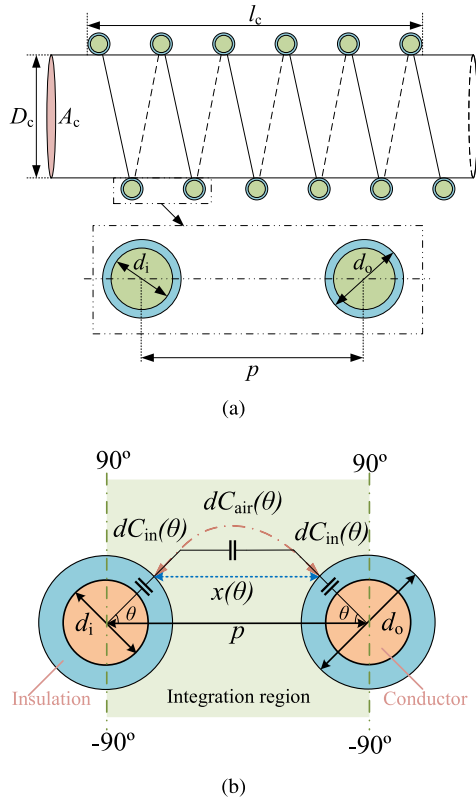
FIGURE 1. (a) Diagram of the single-layer air-core solenoid inductor and (b) schematic of elementary capacitances between two turns for the loose winding ($p > d_o$). A tightly winding ideally satisfies that $p = d_o$.

The elementary capacitance ($dC_{tt}(\theta)$) between two circular conductors consists of two components: the elementary capacitance of the insulation coating ($dC_{in}(\theta)$) and the elementary capacitance of the air gap ($dC_{air}(\theta)$), as illustrated in Fig. 1(b). Their derivation follows the definition of parallel plate capacitors [14]. Specifically, for the insulation coating, the elementary capacitance can be derived as follows:

$$dC_{in}(\theta, l, r) = \varepsilon_r \varepsilon_0 \frac{(rd\theta)\, dl}{dr} \tag{1}$$

$$dC_{in}(\theta) = \int_0^{l_t} \int_{\frac{d_i}{2}}^{\frac{d_o}{2}} dC_{in}(\theta, l, r)$$

$$= \varepsilon_r \varepsilon_0 \, d\theta \int_0^{l_t} dl \int_{\frac{d_i}{2}}^{\frac{d_o}{2}} \frac{r}{dr} = \frac{\varepsilon_r \varepsilon_0 \, l_t}{\ln \frac{d_o}{d_i}} d\theta \tag{2}$$

where, ε_r represents the relative permittivity of the insulation coating, while ε_0 denotes the permittivity of vacuum. The length of one turn, denoted as l_t, is equal to $\pi(D_c + d_o)$. D_c represents the diameter of the bobbin where the inductor is wound. The d_i and d_o refer to the diameters of the bare conductor and the conductor with insulation, respectively.

Similarly, the elementary capacitance for the air gap based on the definition of parallel plate capacitors can be computed by:

$$dC_{air}(\theta) = \varepsilon_0 \frac{l_t \left(\frac{d_0}{2} d\theta\right)}{x(\theta)} \tag{3}$$

where $x(\theta)$ represents the path of the electric field between two turns, with its length dependent on the θ as depicted in Fig. 1(b). Some studies assume a straight line for this path [15] (dashed blue line in Fig. 1(b)), while others use an arc (dash-dot red curve in Fig. 1(b)) [18]. The impact of these different choices will be discussed in Section III. Accordingly, $x(\theta)$ can be expressed as:

$$x(\theta) = \begin{cases} p - d_o \cos\theta & \text{straight line} \\ (p - d_o \cos\theta)\dfrac{\theta}{\sin\theta} & \text{arc} \end{cases} \tag{4}$$

where p represents the pitch distance between turns measured from the center points of the turns. It is worth mentioning that the above equations are valid for both tightly winding ($p = d_o$) and loose winding ($p > d_o$) conditions.

The total elementary capacitance $dC_{tt}(\theta)$ is calculated by the series connection of two $dC_{in}(\theta)$ and one $dC_{air}(\theta)$:

$$dC_{tt}(\theta) = \frac{dC_{air}(\theta)\frac{dC_{in}(\theta)}{2}}{dC_{air}(\theta) + \frac{dC_{in}(\theta)}{2}} = \frac{\varepsilon_0\, l_t}{2\left(\frac{x(\theta)}{d_0} + \frac{1}{\varepsilon_r}\ln\frac{d_o}{d_i}\right)} d\theta \tag{5}$$

The turn-to-turn capacitance C_{tt} can be determined by integrating the elementary capacitance $dC_{tt}(\theta)$ over the range from $-\pi/2$ to $\pi/2$ as depicted in Fig. 1(b) by [15]:

$$C_{tt} = \int_{-\frac{\pi}{2}}^{\frac{\pi}{2}} \frac{\varepsilon_0 l_t}{2\left(\frac{x(\theta)}{d_o} + \frac{1}{\varepsilon_r}\ln\frac{d_o}{d_i}\right)} d\theta \tag{6}$$

It should be noted that a narrower integration range (e.g., from $-\pi/6$ to $\pi/6$) needs to be considered when the turns are surrounded by other turns, in order to take into account the proximity effects observed in inner turns of multi-layer air-core inductors discussed in Section III.

B. TOTAL STRAY CAPACITANCE
In the second step, the total self-capacitance (C_{tot}) responsible for the first SRF of the inductor is evaluated. To this end, two methods can be used: the physical-based analytical method and the empirical-based expression.

1) PHYSICAL-BASED ANALYTICAL METHOD
The physical-based analytical method can be implemented by two approaches: the lumped-capacitance network method [14] and the energy-conservation method [10]. Anyhow, both methods assume the mutual coupling between adjacent turns to be dominant over the mutual coupling between non-adjacent turns, which is therefore neglected. Additionally, the inductive coupling among all turns is also neglected.

Moreover, the lumped-capacitance network method considers the equivalent circuit of the inductor as a purely capacitive network composed of C_{tt}, disregarding the elementary inductance (L_{tt}) of each turn due to its high impedance compared to C_{tt}. On the other hand, the energy-conservation method takes into account the effect of the elementary inductance and assumes a linear voltage distribution along
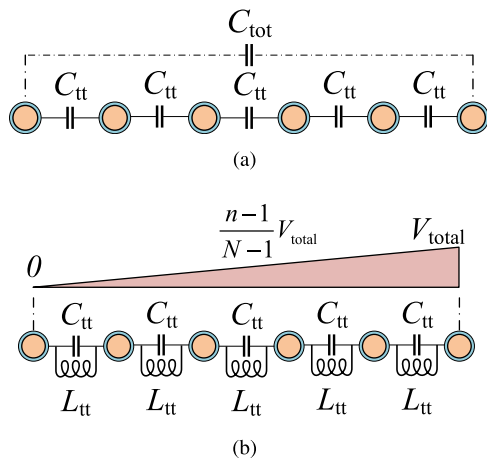
FIGURE 2. Equivalent circuit based on (a) lumped-capacitance network method and (b) energy-conservation method.

the coils [11]. Consequently, the total stray capacitance C_{tot} can be calculated by equating the energy of the electric field stored in C_{tot} to the total energy stored between all turns.

The comparison in [11] shows that the energy-conservation method is more accurate than the lumped-capacitance network method when a toroid inductor with a ferrite core is modeled. However, this conclusion may only apply to inductors with ferrite cores. As a matter of fact, when applying these two methods to a single-layer air-core inductor, the turn-to-core capacitance does not exist. Consequently, both methods yield the same equations to calculate the stray capacitance $C_{tot} = C_{tt}/(N - 1)$.

According to the equivalent circuit approach, the initial step involves the evaluation of the turn-to-turn capacitance C_{tt} by utilizing equations (1) through (6). Fig. 2(a) illustrates the equivalent circuit of an inductor with N turns (here $N = 6$), assuming a lumped-capacitance network. In this configuration, $N - 1$ turn-to-turn capacitances (C_{tt}) are connected in series. Consequently, employing this approach takes the expression of the total stray capacitance C_{tot}:

$$C_{tot}(N) = \frac{C_{tt}}{N - 1} \quad (7)$$

The equivalent circuit of the single-layer air-core inductor derived according to the energy-conservation approach is shown in Fig. 2(b). It is assumed that the voltage potential is linearly distributed across all turns due to the inductance associated with each turn. Hence, the voltage potential of the n-th turn is $[V_{total}(n - 1)]/(N - 1)$, and the voltage drop between two adjacent turns is $V_{total}/(N - 1)$. Here, V_{total} represents the voltage applied between the first and last turn of the inductor. Moreover, the electric-field energy stored in the total self-capacitance C_{tot} is considered equivalent to the total energy stored between all turns. Based on this assumption, the total stray capacitance can be derived as:

$$C_{tot}(N) = \sum_{n=1}^{N-1} \left(\frac{V_{total}}{N - 1}\right)^2 \frac{C_{tt}}{V_{total}^2} = \frac{C_{tt}}{N - 1} \quad (8)$$

Differently from the case of a toroid ferrite-core inductor [11], both methods yield the same equation for single-layer air-core inductors. However, both (7) and (8) indicate that the total stray capacitance decreases as the number of turns N increases, and approaches zero for N taking an infinite value. This is not realistic since the stray capacitance of an inductor with a large number of turns is anyway expected to be non-negligible.

2) EMPIRICAL-BASED METHOD
In contrast to the physical-based analytical methods, the empirical approach relies on a series of measurements and/or simulations conducted on several inductor samples featuring various specifications. Through curve-fitting procedures applied to different parameters, such as inductor length (l_c), bobbin diameter (D_c), and pitch distance (p), an empirical formula for the stray capacitance can be derived. Particularly, the empirical formula in [7] and [19], is adapted here to predict the stray capacitance of a single-layer air-core inductor:

$$C_{tot} = \frac{4\varepsilon_0 \, l_c}{\pi} \left\{ 0.18\frac{D_c}{l_c} + 0.25 + 0.6\left(\frac{D_c}{l_c}\right)^{1.5} \right\} \quad (9)$$

Accuracy of the proposed expressions will be investigated in the following subsection.

C. MEASUREMENT VERIFICATION
In order to verify the accuracy of the methods discussed in previous sections, an inductor sample is created by winding an insulated copper conductor (diameters of the bare conductor and with insulation coating are $d_i = 2.65$ mm, and $d_o = 2.7$ mm, respectively) on a cylindrical polyvinyl chloride (PVC) core. The relative permittivity of the polyester coating ε_r ranges from 2.8 to 4.5. Other parameters of the inductor sample are the diameter of the PVC bobbin $D_c = 103.2$ mm, the pitch between turns $p = 2d_o = 5.4$ mm, and the number of turns $N = 33$. The impedance of the inductor is measured using an impedance analyzer (Keysight E4990A, 20 Hz to 120 MHz). Measurements were repeated by progressively removing turns until only two turns remained.

To provide a reference, the circuit model of the inductor (with the self-capacitance (C_{tot}) in parallel with the series of an inductor (L) and a resistor) is considered, whose parameters were obtained by fitting of the measured impedance, after de-embedding from measurement data spurious effects due to inductor leads.

To validate the fitted circuit model, the inductance L of the single-layer air-core inductor is preliminarily computed by [20]:

$$L = \frac{\mu_0 \, A_c N^2}{l_c K} \quad (10)$$

where μ_0 represents the permeability of free space, $A_c = \pi (D_c/2)^2$ denotes the cross-sectional area of the bobbin, $l_c = (N - 1)p + d_o$ represents the length of the inductor,
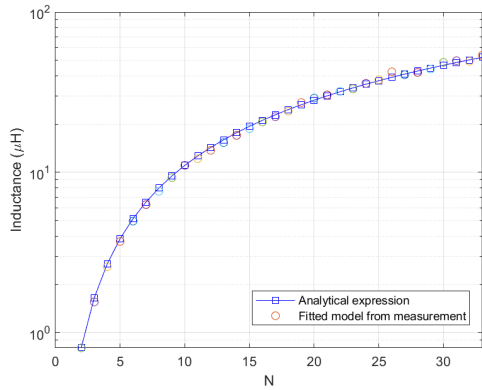
(a)
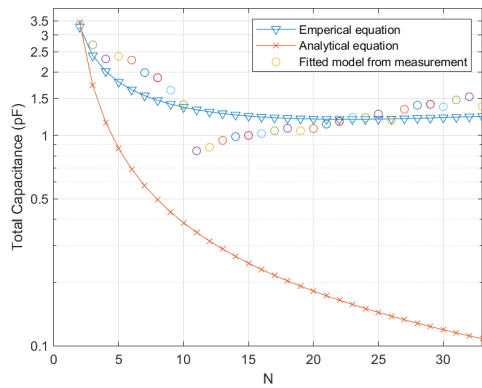
(b)

FIGURE 3. Comparison of prediction and fitted circuit model based on measurement for (a) inductance (*L*) and (b) stray capacitance (*C*tot) under different turn *N* numbers.

and *K* is the Nagaoka's coefficient defined as $K = 1 + 0.9D_c/(2l_c)$ [21].

For each inductor sample, the inductance computed by (10) is compared with the inductance in the fitted circuit model as illustrated in Fig. 3(a). The close agreement observed validates the accuracy of the fitted circuit model. The C_{tot} within this circuit model will serve as reference to evaluate the accuracy of the physical-based analytical method and the empirical formula, as depicted in Fig. 3(b).

As shown in Fig. 3(b), the analytical model exhibits a decreasing trend, leading to significant deviations from the reference for large turn numbers. Specifically, when *N* exceeds 30, the predictions of the analytical equation are approximately 13 times smaller than the measurement. The significant deviation introduced by the physical-based analytical approaches, either based on the energy-conservation method or the lumped-capacitance network, makes these methods unsuitable for estimating the stray capacitance of single-layer air-core inductors. On the other hand, the empirical approach consistently delivers relatively accurate results in line with the measurements. Therefore, this approach will be hereinafter adopted for optimal design of single-layer air-core inductors under practical constraints, as detailed in Section IV.
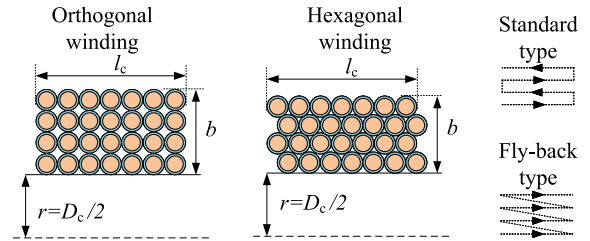
FIGURE 4. Winding types for multi-layer air-core inductors.

III. MODELING METHODS FOR MULTI-LAYER INDUCTORS

A. FIVE FACTORS IN TURN-TO-TURN CAPACITANCE

Similar to single-layer inductors, stray capacitances of multi-layer inductors are assumed to be induced by adjacent current loops, while disregarding the effect of non-adjacent loops. However, in the case of multi-layer air-core inductors, besides the turn-to-turn capacitance (C_{tt}) within each layer, the capacitance between layers (C_{ll}) should be taken into account. The total stray capacitance depends on the geometric parameters of conductors (i.e., the diameter of bare conductors d_i, the coating conductors d_o, and the relative permittivity of insulation material ε_r), as well as the coil parameters (including the number of layers N_l, the number of turns in each layer N_m, and the bobbin diameter D_c) and the winding types [13].

The common winding types for orthogonal and hexagonal wire arrangement are illustrated in Fig. 4. For the construction of multi-layer inductors, the standard type rather than the fly-back type is employed. However, due to the geometric uncertainties associated with numerous layers, maintaining a purely orthogonal or hexagonal winding type is a difficult construction. Consequently, modeling procedures for both orthogonal and hexagonal windings are established to define reference cases for the evaluation of the actual stray capacitances.

The expression in (6) for the elementary capacitance of adjacent turns (C_{tt} and C_{ll}) is here generalized as:

$$C_{tt/ll} = \int_{\theta_1}^{\theta_2} \frac{\varepsilon_0 \, l_x}{2 \left(\frac{x(\theta)}{d_0} + \frac{1}{\varepsilon_{eff}} \ln \frac{d_o}{d_i} \right)} d\theta \qquad (11)$$

where the accuracy of computed elementary capacitance can be affected by five key parameters: (1) the integration range (θ_1 to θ_2), (2) the turn length, l_x, (3) the effective permittivity of the insulation coating, ε_{eff}, (4) the choice of using straight lines or arc curve to represent the electric field path, $x(\theta)$, and (5) the pitch, *p*.

Indeed, different integration ranges for the inner turns (which are surrounded only by the other turns) and the outer turns (which are surrounded by other turns and air) are considered in [13]. However, the turn length l_x is typically considered as the average turn length. In fact, as the number of layers increases, the top turns have a greater length compared to the bottom turns. Therefore, in order to take both factors into consideration, this study proposes an accurate approach

TABLE 1. Predicted capacitances for the three cases in Fig. 5.

No.	Simulation (pF)	Conventional Method			Proposed Method		
		Integration range	Predictions (pF)	Deviations (pF)	Integration range	Predictions (pF)	Deviations (pF)
Case 1	109.1			21.7	-90° to 90°	109.4	-0.3
Case 2	94.6	-30° to 30°	87.4	7.2	-90° to 30°	98.4	-3.8
Case 3	87.9			0.5	-30° to 30°	87.4	0.5
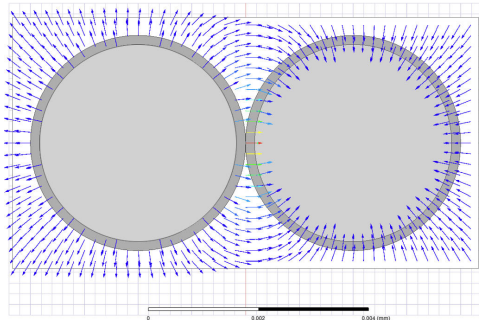
(a)
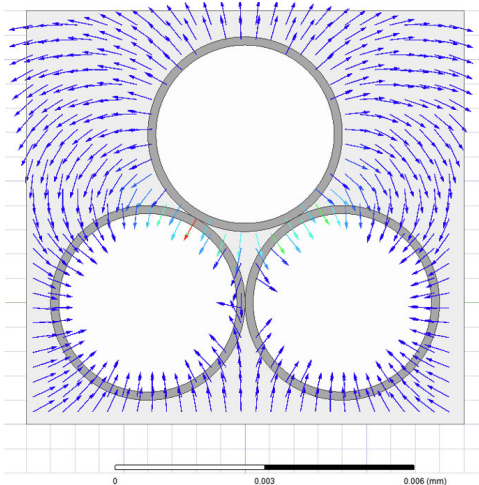
(b)
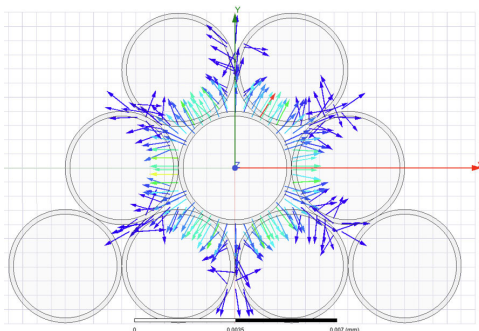
(c)

FIGURE 5. Electric field distribution for two circular conductors in Ansys: (a) case 1: in the absence of other conductors, (b) case 2: in the presence of the third conductor, and (c) case 3: surrounded by outer conductors.

to compute the element capacitance in multi-layer inductors. The choice of using a straight line or arc to represent $x(\theta)$, as well as the uncertainties associated with ε_{eff} and p, will be investigated in Section V.
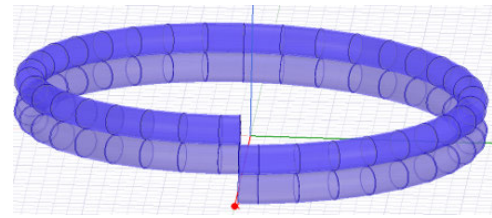
FIGURE 6. 3D model of two turns in Ansys for computing mutual capacitance.

TABLE 2. Predicted capacitance of two turns (3D model) with different turn length.

Diameter of bobbin D_c (mm)	Simulation (pF)	Predictions (pF)	Deviations (pF)
55	21.5	21.1	0.4
75	28.7	28.2	0.5
95	35.5	35.3	0.2

To prove the need to consider different integration ranges for the inner and outer turns to account for proximity effects, the capacitance between two circular elements is simulated in Ansys Maxwell [22] for three test cases (refer to Fig. 5): Case 1: Two conductors only, Case 2: Three conductors in hexagonal geometry, Case 3: Nine conductors in hexagonal geometry. These cases will serve as reference to assess the accuracy of the conventional integration range (−30° to 30° for all cases) compared to the proposed approach in which different integration ranges for the inner and outer turns are considered. The comparison (see Table 1) proves the influence of the proximity effect caused by the surrounding conductors, and the need for taking it into account by utilizing different integration ranges.

To justify the need to consider varying turn lengths in multi-layer air-core inductors, a 3D model is simulated in Ansys Maxwell [22], featuring two turns with different bobbin diameters (see Fig. 6). The stray capacitances obtained from the simulation are compared with the predictions calculated by (11), as shown in Table 2. The results indicate a good agreement between predictions and simulation outcomes. Furthermore, it is observed that the stray capacitance increases with the turn length, thereby confirming the importance of accounting for different turn lengths in multi-layer inductors.

B. TOTAL STRAY CAPACITANCE FOR DIFFERENT WINDINGS TYPES

In this subsection, the energy-conservation method is adopted to derive the total stray capacitance of multi-layer air-core inductors. Considering geometric uncertainties, actual
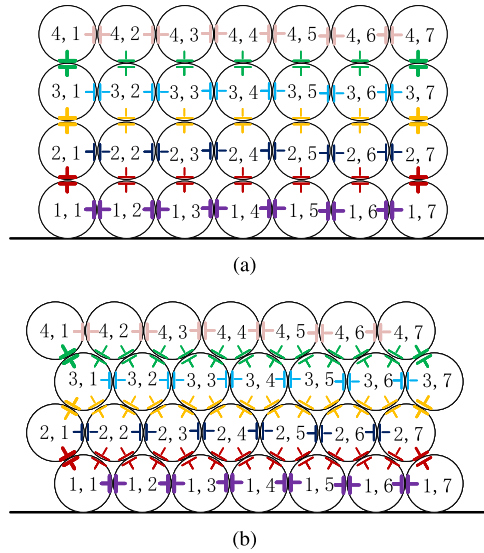
FIGURE 7. Cross sections of multi-layer inductors (a) orthogonal, and (b) hexagonal winding type, with turn-to-turn capacitances (C_{tt}) and layer-to-layer capacitances (C_{ll}) outlined.

multi-layer inductors do not strictly adhere to either orthogonal or hexagonal winding types. Consequently, accurate modeling of actual wire arrangements is a challenge. Instead of focusing on a specific realization, we will investigate the variability of the stray capacitance associated with both geometries in order to provide estimates of the possible variability range.

Fig. 7 provides a comparison of the cross sections of multi-layer inductors created using two different winding types. Each turn is designated as (k, i), where k represents the k-th layer, and i represents the i-th turn within the k-th layer from left to right. Assuming the inductor comprises N_l layers and N_m turns per layer, there are $N_m - 1$ turn-to-turn capacitances C_{tt} in N_l layers for both orthogonal and hexagonal winding types. Regarding layer-to-layer capacitances (C_{ll}), the orthogonal and hexagonal winding types have N_m and $2N_m - 1$ stray capacitances, respectively.

Turn-to-turn capacitances are denoted as $C_{tt}(k, i)$, where k ranges from 1 to N_l and i ranges from 1 to $N_m - 1$, for both winding types. Layer-to-layer capacitances are denoted as $C_{ll}(k, i)$, where k ranges from 1 to $N_l - 1$, and for orthogonal winding, i ranges from 1 to N_m, while for hexagonal winding, i ranges from 1 to $2N_m - 1$.

The turn length l_x for $C_{tt}(k, i)$ and $C_{ll}(k, i)$ are denoted as l_{tt} and l_{ll}, respectively, and are the same for turns within the same layer. Turn length l_x is given by:

$$\begin{cases} l_{tt}(k) = \pi \left[D_c + (2k - 1) d_o \right] \\ k = 1, 2, 3, \ldots, N_l \end{cases}$$
$$\begin{cases} l_{ll}(k) = \pi \left(D_c + 2k d_o \right) \\ k = 1, 2, 3, \ldots, N_l - 1 \end{cases} \tag{12}$$

for orthogonal winding, and by:

$$\begin{cases} l_{tt}(k) = \pi \left[D_c + d_o + \sqrt{3} \left(k - 1 \right) d_o \right] \\ k = 1, 2, 3, \ldots, N_l \end{cases}$$
$$\begin{cases} l_{ll}(k) = \pi \left[D_c + d_o + \dfrac{\sqrt{3}}{2} \left(2k - 1 \right) d_o \right] \\ k = 1, 2, 3, \ldots, N_l - 1 \end{cases} \tag{13}$$

for hexagonal winding.

To account for the proximity effect, the turn-to-turn capacitance C_{tt} in the top and bottom layers and the layer-to-layer capacitance C_{ll} in the first and last column, respectively, separately from the other inner layers, is defined by:

$$C_{tt}(k, i) = \int_{\theta_1}^{\theta_2} \frac{\varepsilon_0 \, l_{tt}(k)}{2 \left(\frac{x(\theta)}{d_o} + \frac{1}{\varepsilon_{\text{eff}}} \ln \frac{d_o}{d_i} \right)} d\theta$$
$$\begin{cases} k = 1, N_l \\ i = 1, 2, 3, \ldots, N_m - 1 \end{cases} \tag{14}$$

$$C_{ll}(k, i) = \int_{\theta_1}^{\theta_2} \frac{\varepsilon_0 \, l_{ll}(k)}{2 \left(\frac{x(\theta)}{d_o} + \frac{1}{\varepsilon_{\text{eff}}} \ln \frac{d_o}{d_i} \right)} d\theta$$
$$\begin{cases} k = 1, 2, 3, \ldots, N_l - 1 \\ i = 1, N_m & \text{(orthogonal)} \\ i = 1, 2N_m - 1 & \text{(hexagonal)} \end{cases} \tag{15}$$

where different integration ranges, i.e., $[-\pi/2, \pi/4]$ and $[-\pi/2, \pi/6]$, are used for the orthogonal and hexagonal windings, respectively, as explained in Section III-A.

For the remaining inner capacitances, the following expressions are cast:

$$C_{tt}(k, i) = \int_{\theta_1}^{\theta_2} \frac{\varepsilon_0 l_{tt}(k)}{2 \left(\frac{x(\theta)}{d_o} + \frac{1}{\varepsilon_{\text{eff}}} \ln \frac{d_o}{d_i} \right)} d\theta$$
$$\begin{cases} k = 2, 3, \ldots, N_l - 1 \\ i = 1, 2, 3, \ldots, N_m - 1 \end{cases} \tag{16}$$

$$C_{ll}(k, i) = \int_{\theta_1}^{\theta_2} \frac{\varepsilon_0 \, l_{ll}(k)}{2 \left(\frac{x(\theta)}{d_o} + \frac{1}{\varepsilon_{\text{eff}}} \ln \frac{d_o}{d_i} \right)} d\theta$$
$$\begin{cases} k = 1, 2, 3, \ldots, N_l - 1 \\ i = 2, 3, \ldots, N_m - 1 & \text{(orthogonal)} \\ i = 2, 3, \ldots, 2N_m - 2 & \text{(hexagonal)} \end{cases} \tag{17}$$

with integration ranges $[-\pi/4, \pi/4]$ and $[-\pi/6, \pi/6]$ for the orthogonal and hexagonal windings, respectively.

The voltage difference between two adjacent turns within the same layer is $U_{tt} = V_{\text{total}}/(N - 1)$ for both winding types. V_{total} denotes the total voltage applied across the two terminals of the inductor. Conversely, the voltage difference between two turns in adjacent layers tales different expressions:

$$U_{ll}(k, i) = \frac{(2i - 1) V_{\text{total}}}{N - 1} \quad \text{(orthogonal)}$$

$$\begin{cases} k = 1, 2, 3, \ldots, N_1 - 1 \\ i = 1, 2, 3, \ldots, N_m \end{cases} \quad (18)$$

$$U_{ll}(k, i) = \frac{iV_{total}}{N - 1} \quad \text{(hexagonal)}$$

$$\begin{cases} k = 1, 2, 3, \ldots, N_1 - 1 \\ i = 1, 2, 3, \ldots, 2N_m - 1 \end{cases} \quad (19)$$

for orthogonal and hexagonal windings, respectively.

Based on the energy-conservation theorem, the energy stored in the overall stray capacitance C_{tot} is equivalent to the sum of the energy stored between turns and between layers. Consequently, C_{tot} for the orthogonal and hexagonal windings with standard winding configuration read:

$$C_{tot(orthogonal)} = \frac{1}{(N-1)^2} \left[\sum_{k=1}^{N_1} \sum_{i=1}^{N_m-1} C_{tt}(k, i) \right.$$
$$\left. + \sum_{k=1}^{N_1-1} \sum_{i=1}^{N_m} (2i-1)^2 C_{ll}(k, i) \right] \quad (20)$$

$$C_{tot(hexagonal)} = \frac{1}{(N-1)^2} \left[\sum_{k=1}^{N_1} \sum_{i=1}^{N_m-1} C_{tt}(k, i) \right.$$
$$\left. + \sum_{k=1}^{N_1-1} \sum_{i=1}^{2N_m-1} i^2 C_{ll}(k, i) \right] \quad (21)$$

IV. EXAMPLE 1: DESIGN OF A SINGLE-LAYER INDUCTOR

The CISPR 16-1-2 standard specifies an AC LISN with a defined impedance (50 μH + 5 Ω) ‖ 50 Ω for the frequency range from 9 kHz to 30 MHz. A key component in the LISN design is the 50 μH inductor, typically designed as a single-layer air-core inductor to prevent saturation when carrying high currents. AC LISN performance is significantly influenced by the characteristics of such an inductor, which should have a small stray capacitance (i.e., high SRF) to ensure a stable LISN impedance and effective decoupling at high frequencies. According to [15], increasing the pitch distance p leads to a higher SRF. However, this benefit is marginal with a large pitch, which can also lead to an extended inductor length. On the other hand, it is also desirable to keep the inductor dimensions as small as possible to suit the LISN volume. This section is aimed at a procedure for optimal design of a 50 μH single-layer air-core inductor, taking into account the requirements of higher SRF and smaller volume (i.e., smaller bobbin diameter D_c and length l_c). To this end, the equations for the stray capacitance in (9) and the inductance in (10) will be exploited.

The procedure involves determining the number of turns N and the pitch p while setting L to 50 μH and imposing constraints on the SRF, D_c, and l_c. To ensure the required LISN performance at high frequencies, the SRF is chosen to be at least 20 MHz. The maximum length of the bobbin core is limited to 180 mm to ensure it fits within the LISN volume. Three diameters of PVC bobbins (D_c) are considered: 50 mm, 100 mm, and 150 mm.

All feasible configurations of inductors having 50 μH inductance are determined through parameter sweeps, that

TABLE 3. 50 μH single-layer air-core inductor: Expected vs measured parameters.

Parameter	Expected	Measured
d_i (mm)	2.65	2.65
d_o (mm)	2.70	2.70
p (mm)	5.4	average: 5.4
D_c (mm)	103.2	103.2
N	33	33
l_c (mm)	175.5	175
L (μH)	51.6	51.5
C_{tot} (pF)	1.2	1.4
SRF (MHz)	19.9	18.5

is, by varying the number of turns N from 10 to 90 and the ratio p/d_o from 1.1 to 4 with a step size of 0.1 (see Fig. 8). The solution plane in Fig. 8 illustrates the solution region assuring a 50 μH inductance. Specifically, the red region corresponds to inductors with SRF above 20 MHz, the blue grid region is associated with the inductor length l_c smaller than 180 mm, and the green/black regions correspond to three options for the bobbin diameter: approximately 50 mm, 100 mm, and 150 mm, respectively.

In general, a smaller bobbin diameter D_c with long inductor length l_c results in a higher SRF (see the black region labeled as $D_c = (50 \pm 3)$ mm). On the contrary, a larger bobbin diameter requires a smaller number of turns (i.e., shorter inductor length) to achieve the desired 50 μH inductor, but the SRF will be reduced significantly. Therefore, the optimal design is the one balancing the requirement of high SRFs and compact inductor volume. As a tradeoff, the highlighted configuration in Fig. 8 is selected, where: the SRF is around 20 MHz, the $N = 33$, $p = 2d_o = 5.4$ mm, $D_c = 101$ mm, and $l_c = 175.5$ mm.

To verify the previous design by measurement, an inductor prototype was realized, exploiting a PVC with outer diameter $D_c = 103.2$ mm. It is wound with 33 turns, resulting in an inductance of 51.6 μH. The computed stray capacitance C_{tot} is 1.2 pF, and the computed SRF is 19.9 MHz. The inductance and stray capacitance of the prototype are obtained by fitting the input impedance of the prototype measured by an impedance analyzer through an RLC circuit model [1]. Table 3 compares expected parameters and the measured data for the inductor, revealing an excellent agreement.

V. EXAMPLE 2: DESIGN OF A MULTI-LAYER INDUCTOR

This section presents a two-step procedure for the optimal design of a multi-layer air-core inductor, considering constraints on inductance, SRF, and size. In the first step, the specifications of the inductor are determined based on three available bobbin diameters, taking into account the desired inductance (hereinafter, 670 μH). In the second step, the stray capacitances of the three designed inductors are estimated using the proposed analytical model in Section III.
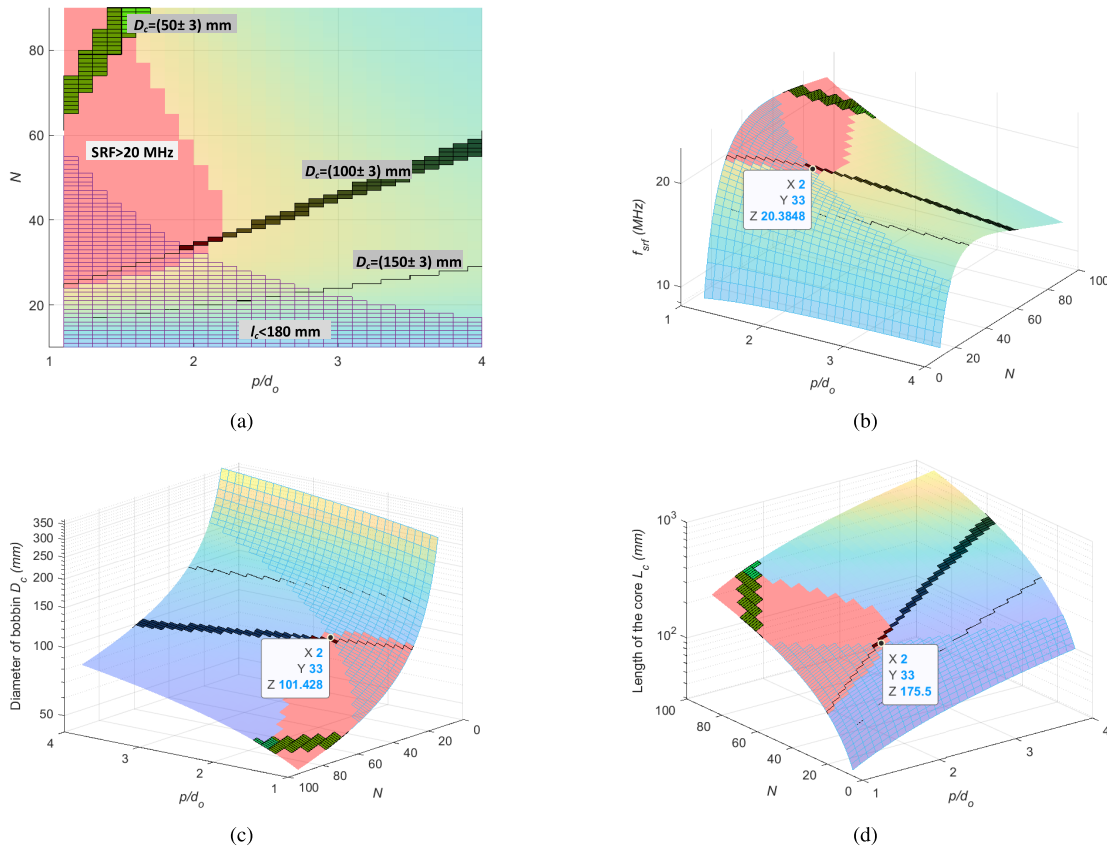
FIGURE 8. 50 μH single-layer air-core inductor: (a) notation for each region, and optimal design based on (b) SRF, (c) diameter of bobbin D_c, and (d) length of inductor l_c.
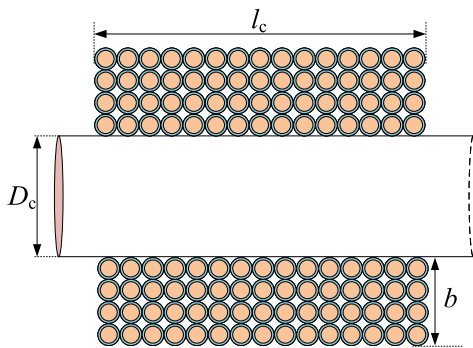
FIGURE 9. Principle diagram of a multi-layer air-core inductor.

A. DESIGN BASED ON BOBBIN DIAMETER AND INDUCTANCE

From the Wheeler's approximation, the inductance of a multi-layer solenoid inductor is given by [23]:

$$L = \frac{31.6 N^2 r^2}{6r + 9l_c + 10b} \times 10^{-6} \quad (22)$$

where: $r = D_c/2$ is the radius of the bobbin, l_c is the length of the inductor, and b is the overall width. This formula applies at low frequency (below 3 MHz) and assumes the use of tightly wound insulated copper wire, yielding an inaccuracy of $< 1\%$ if the cross-section is nearly square-shaped. Specifically, if the inductor consists of N_l layers, this

formula is applicable if all layers have the same number of turns, denoted as N_m. In such cases, the coil width can be computed as $b = N_l d_o$, the coil length is given by $l_c = N_m d_o$, and the total number of turns is determined as $N = N_m N_l$ (See Fig. 9 for the diagram of a multi-layer inductor).

TABLE 4. 670 μH multi-layer air-core inductor: Specifications for different bobbin diameters.

D_c (mm)	N_l	N_m	l_c (mm)	b (mm)	L (μH)
100	8	10	27.0	21.6	666.1
150	7	8	21.6	18.9	668.9
200	5	9	24.3	13.4	671.0

The multi-layer inductor is wound using wires of the same type ($d_i = 2.65$ mm, $d_o = 2.7$ mm) with the same characteristics as those used for the single-layer inductor. By taking into account three distinct bobbin diameters D_c (100 mm, 150 mm, and 200 mm), specifications for each bobbin diameter are computed to achieve an inductance closest to 670 μH (see Table 4).

B. SRF PREDICTION CONSIDERING UNCERTAINTY FACTORS

In the second step, the proposed modeling procedures for both orthogonal and hexagonal winding types are adopted to account for the uncertainties associated with the winding geometry. These procedures are used to estimate the range
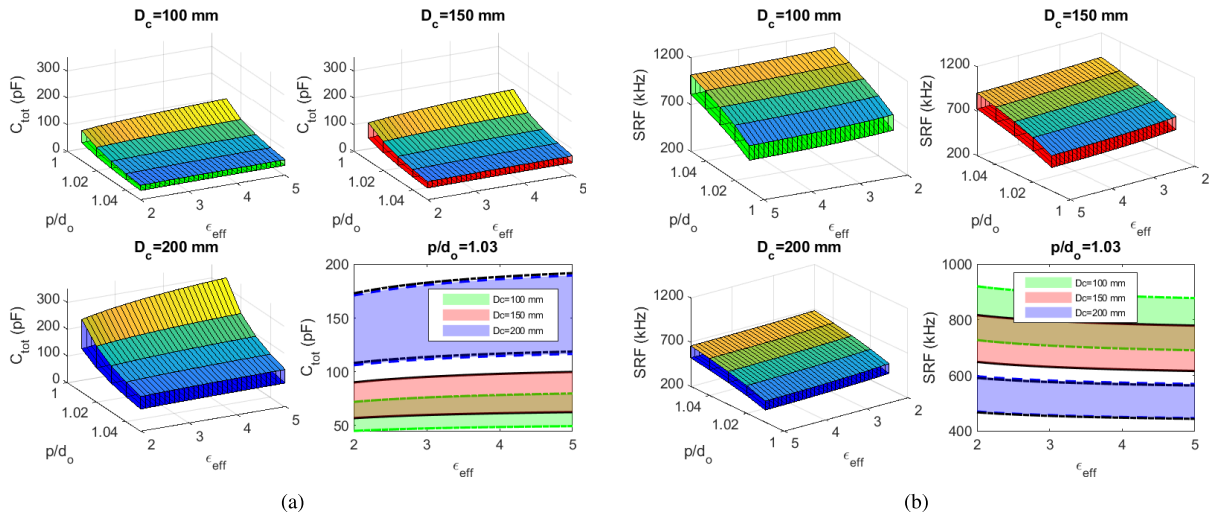
FIGURE 10. Predicted (a) stray capacitances and (b) SRF considering the uncertainty of winding type, winding tightness (p/d_o), and the permittivity of coating material (ε_{eff}) for three inductors in Table 4.
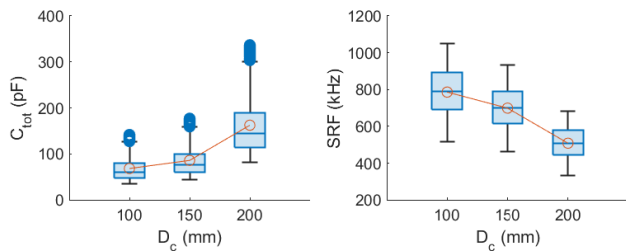
FIGURE 11. Box plots showing the predicted stray capacitances and SRFs for three 670 μH multi-layer air-core inductors assuming uniform distributions for the parameters ($p - d_o$) and ε_{eff}.

TABLE 5. Statistics of predictions for the stray capacitance and SRF of the 670 μH multi-layer air-core inductors with different bobbin diameters.

D_c (mm)	Prediction	First quartile	Median	Mean	Third quartile
100	C_{tot} (pF)	36.9	47.4	50.4	58.7
150		46.8	59.7	63.4	73.8
200		87.4	112.6	119.7	139.6
100	SRF (kHz)	804.6	895.7	903.0	1015.0
150		716.2	796.8	802.7	900.2
200		520.1	579.2	584.1	657.3

of variability of the stray capacitance and SRF for the three inductors in Table 4. Additionally, the effects of other factors, i.e., p, ε_{eff}, and $x(\theta)$ are investigated.

Concerning the uncertainties related to winding tightness and the permittivity of the insulation material, the variability of the stray capacitances and SRF under different p/d_o and ε_{eff} is illustrated in Fig. 10(a) and (b), respectively. For each D_c, the stray capacitances for the orthogonal and hexagonal winding types correspond to the bottom and upper boundary of the 3D region in Fig. 10(a).

The results put in evidence the significant influence of the pitch p. The total stray capacitance decreases as p increases, although this benefit becomes less pronounced for a larger value of p. Due to the uncertainty in winding tightness, it is hard to keep the value of p constant at the nominal value $p = d_o$. Therefore, the distance between the wire periphery

of two turns ($p - d_o$) is indirectly measured and afterward modeled by a uniformly distributed parameter: $p - d_o \sim U[0.052 \text{ mm}, 0.208 \text{ mm}]$.

Regarding the relative permittivity of coating material ε_{eff}, an example is illustrated in Fig. 10(a) (bottom right panel), demonstrating that the stray capacitance increases with high values of ε_{eff}. This is more evident when p is small, and emphasizes the importance of accurately determining the effective permittivity of the coating, although only rough information on this parameter is usually provided by the manufacturers. For the used copper wire, the exact relative permittivity ε_{eff} of the polyester coating is not specified in the datasheet, where only a range of variation from 2.8 to 4.5 is indicated [16], [17]. Thus, a uniform distribution $\varepsilon_{eff} \sim U[2.8, \ 4.5]$ is hereinafter assumed for this parameter.

An arc curve of $x(\theta)$ is assumed for the prediction of the stray capacitance in Fig. 10(a). For the sake of comparison, the capacitance boundaries obtained by assuming a straight electric field path are also plotted (dashed black line) for the $D_c = 200$ mm case (blue block in the bottom right panel in Fig. 10(a)). Remarkably, the computed stray capacitances under these two assumptions are nearly identical. In fact, the arc length can be approximated as a straight line when the arc angle is small. Hence, this choice has negligible impact on the capacitance prediction with respect to other sources of uncertainty. As a consequence, the influence on the SRF is also negligible (as shown for the D_c =200 mm case in the bottom right panel in Fig. 10(b)).

In summary, the uncertainties mostly influencing the SRF are those related to the winding type (orthogonal, hexagonal), the winding tightness (p/d_o), and the effective permittivity of coating material (ε_{eff}).

Assuming $p - d_o \sim U[0.052 \text{ mm}, 0.208 \text{ mm}]$ and $\varepsilon_{eff} \sim U[2.8, \ 4.5]$, 100,000 uniformly-random pairs of (p, ε_{eff}) are used for prediction of both orthogonal and hexagonal winding types. The box plots in Fig. 11 show the variability of the inductor stray capacitance and SRF for

TABLE 6. Specifications of the multi-layer air-core inductor: designed values vs. measurement of prototype.

Parameters	Design	Measurement
d_i (mm)	2.65	
d_o (mm)	2.70	
D_c (mm)	150	
N_m	8	from bottom to top:
N_l	7	9-8-8-8-8-8-2
N	53	
l_c (mm)	25	
b (mm)	from 16.73 to 18.90	from 16.63 to 19.06
L (μH)	from 507.9 ($N_m = 8$, $N_l = 6$, orthogonal) to 686.7 ($N_m = 8$, $N_l = 7$, hexagonal)	666.6
C_{tot} (pF)	Median: 60.9 Mean: 64.8 First to third quartiles: 46.6 to 75.8	74.1
SRF (kHz)	Median: 789.6 Mean: 798.4 First to third quartiles: 708.2 to 903.3	716.3
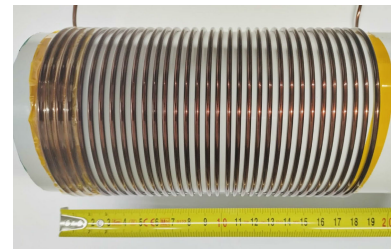
(a)

(b)

FIGURE 13. Inductor prototypes: (a) Single-layer inductor and (b) Multi-layer air-core inductor.
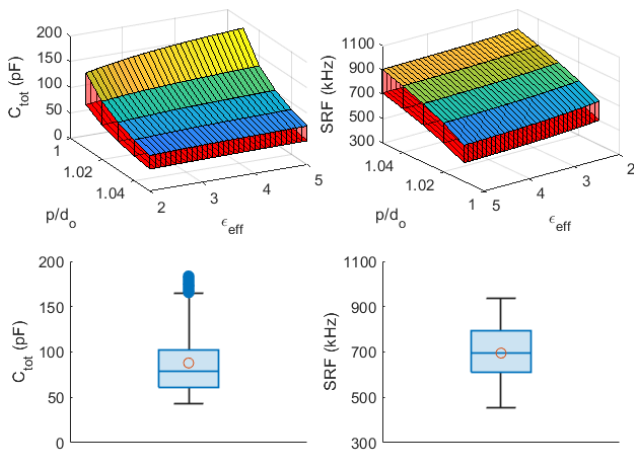
FIGURE 12. Predictions of stray capacitance and SRF for the prototype of the multi-layer air-core inductor.

FIGURE 14. Impedance measurement setup for the multi-layer air-core inductor prototype.

each bobbin diameter, based on a total number of 200,000 samples. Relevant statistical estimates are summarized in Table 5.

Based on the statistical analysis, the inductor design with bobbin diameter $D_c = 150$ mm is selected, striking a balance between SRF and other constraints. Specifically, although the smallest inductor ($D_c = 100$ mm) exhibits a higher SRF (with a median of 895.7 kHz), it requires over 40% more turns compared to $D_c = 150$ mm (see Table 5). On the other hand, the inductor with $D_c = 200$ mm requires 20% turns less, but its SRF is significantly reduced (the first quartile is 520.1 kHz).

C. VALIDATION VERSUS MEASUREMENT
To validate previous predictions by measurement, an inductor prototype is designed with a bobbin diameter $D_c = 150$ mm,

number of layers $N_l = 7$, and number of turns in each layer $N_m = 8$ (see Table 4). Due to construction constraints for fixing turn positions, in the prototype, the actual number of turns varies for each layer as summarized in Table 6. The two prototypes and the impedance measurement setup are shown in Fig. 13 and Fig. 14, respectively. The inductance and stray capacitance of the prototype are obtained following the same data-processing procedure adopted for the single-layer inductor. The procedures for predicting stray capacitances are slightly adjusted to match the specifications of the inductor prototype. The predicted first and third quartiles (see Fig. 12) provide a reliable range of variability for the stray capacitance and SRF, which is verified by the circuit model based on measurements (see Table 6).

VI. CONCLUSION

This paper presents optimal design procedures for single-layer and multi-layer air-core inductors, considering practical engineering constraints, in terms of self-resonant frequency and inductor volume. To this end, prediction models for stray capacitances of single-layer and multi-layer inductors have been thoroughly investigated.

In the case of single-layer air-core inductors, an empirical expression, which is experimentally proved to be more accurate than the physical-based analytical methods, is employed for optimal design procedures. For multi-layer air-core inductors, an enhanced analytical approach based on the energy-conservation method is proposed for both orthogonal and hexagonal winding configurations. This approach considers the impact of five influence factors. Specifically, the proximity effect and the variation in turn length across layers have been identified as key parameters and therefore have been incorporated into the enhanced models. Their impact was investigated by means of FEM simulation and validated by the enhanced models. The other three influence factors (i.e., the electric field path assumption, the effective permittivity of the wire insulation coating, and the winding tightness) are treated as uncertainty factors. Particularly, it was observed that assuming a straight line or an arc curve for the electric field negligibly influences the predicted stray capacitance value. Conversely, the other two factors were proven to significantly affect the prediction of stray capacitance in multi-layer air-core inductors.

To address such uncertainties affecting the geometry and material properties, the proposed design methodology resorts to statistical estimates of the stray capacitance and self-resonant frequency. To assess the effectiveness of the proposed design methodologies, two examples are presented for single- and multi-layer air-core inductors. The fabricated prototypes prove to have characteristics in good agreement with the design specifications.

ACKNOWLEDGMENT

REFERENCES

[1] L. Zhai, S. Yang, G. Hu, and M. Lv, "Design method of wide-band high-current air-core inductor EMI filter for high voltage DC power of motor inverter of electric vehicle," *IET Power Electron.*, vol. 15, no. 15, pp. 1725–1740, Jun. 2022.

[2] R. Barrera-Cardenas, T. Isobe, and M. Molinas, "Optimal design of air-core inductor for medium/high power DC–DC converters," in *Proc. IEEE 17th Workshop Control Model. Power Electron. (COMPEL)*, Jun. 2016, pp. 1–8.

[3] K. Kanzi, M. Kanzi, and H. Nafissi, "VPI varnishing technology effects on frequency characteristics of an air core inductor used in LISN circuit application," *J. Int. Conf. Electr. Mach. Syst.*, vol. 2, no. 1, pp. 57–64, Mar. 2013.

[4] W. N. Fu, S. L. Ho, S. Niu, and J. Zhu, "Comparison study of finite element methods to deal with floating conductors in electric field," *IEEE Trans. Magn.*, vol. 48, no. 2, pp. 351–354, Feb. 2012.

[5] Z. De Grève, O. Deblecker, and J. Lobry, "Numerical modeling of capacitive effects in HF multiwinding transformers—Part II: Identification using the finite-element method," *IEEE Trans. Magn.*, vol. 49, no. 5, pp. 2021–2024, May 2013.

[6] H. Li and W. M. Rucker, "An accurate and efficient hybrid method for the calculation of the equivalent capacitance of an arbitrary-shaped coil," *IEEE Trans. Magn.*, vol. 52, no. 3, pp. 1–4, Mar. 2016.

[7] R. Medhurst, "HF resistance and self-capacitance of single-layer solenoids," *Wireless Eng.*, vol. 24, pp. 35–43, Feb. 1947.

[8] A. Massarini, M. K. Kazimierczuk, and G. Grandi, "Lumped parameter models for single- and multiple-layer inductors," in *Proc. PESC Rec., 27th Annu. IEEE Power Electron. Specialists Conf.*, vol. 1, 1996, pp. 295–301.

[9] G. Grandi, M. K. Kazimierczuk, A. Massarini, and U. Reggiani, "Stray capacitances of single-layer solenoid air-core inductors," *IEEE Trans. Ind. Appl.*, vol. 35, no. 5, pp. 1162–1168, Sep./Oct. 1999.

[10] J. Martínez, S. Babic, and C. Akyel, "On evaluation of inductance, DC resistance, and capacitance of coaxial inductors at low frequencies," *IEEE Trans. Magn.*, vol. 50, no. 7, pp. 1–12, Jul. 2014.

[11] H. Zhao, S. Luan, Z. Shen, A. J. Hanson, Y. Gao, D. N. Dalal, R. Wang, S. Zhou, and S. Munk-Nielsen, "Rethinking basic assumptions for modeling parasitic capacitance in inductors," *IEEE Trans. Power Electron.*, vol. 37, no. 7, pp. 8281–8289, Jul. 2022.

[12] J. Biela and J. W. Kolar, "Using transformer parasitics for resonant converters—A review of the calculation of the stray capacitance of transformers," *IEEE Trans. Ind. Appl.*, vol. 44, no. 1, pp. 223–233, Jan./Feb. 2008.

[13] B. Wu, X. Zhang, X. Liu, and C. He, "An analytical model for predicting the self-capacitance of multi-layer circular-section induction coils," *IEEE Trans. Magn.*, vol. 54, no. 5, pp. 1–7, May 2018.

[14] A. Massarini and M. K. Kazimierczuk, "Self-capacitance of inductors," *IEEE Trans. Power Electron.*, vol. 12, no. 4, pp. 671–676, Jul. 1997.

[15] A. Ayachit and M. K. Kazimierczuk, "Self-capacitance of single-layer inductors with separation between conductor turns," *IEEE Trans. Electromagn. Compat.*, vol. 59, no. 5, pp. 1642–1645, Oct. 2017.

[16] P. A. R. Insulations & Wires Ltd. *Copper Winding Wires*. Accessed: Oct. 26, 2023. [Online.] Available: https://par.uk.com/products/copper-winding-wires

[17] The Engineering ToolBox. *Relative Permittivity—The Dielectric Constant*. Accessed: Oct. 26, 2023. [Online.] Available: https://www.engineeringtoolbox.com/relative-permittivity-d_1660.html

[18] X. Liu, Y. Wang, J. Zhu, Y. Guo, G. Lei, and C. Liu, "Calculation of capacitance in high-frequency transformer windings," *IEEE Trans. Magn.*, vol. 52, no. 7, pp. 1–4, Jul. 2016.

[19] A. Mariscotti, "Determination of the stray capacitance of single layer solenoids," in *Proc. IEEE Int. Instrum. Meas. Technol. Conf.*, May 2011, pp. 1–5.

[20] M. K. Kazimierczuk, *High-Frequency Magnetic Components*. Hoboken, NJ, USA: Wiley, 2009.

[21] H. Nagaoka, "The inductance coefficients of solenoids," *J. College Sci.*, vol. 27, pp. 1–33, Aug. 1909.

[22] *ANSYS Maxwell V15. User's Guide*, ANSYS, Canonsburg, PA, USA, 2011.

[23] H. A. Wheeler, "Simple inductance formulas for radio coils," *Proc. Inst. Radio Eng.*, vol. 16, no. 10, pp. 1398–1400, Oct. 1928.

LU WAN (Member, IEEE) received the double M.Sc. degrees in electrical engineering from Xi'an Jiaotong University, Xi'an, China, and Politecnico di Milano, Milan, Italy, in 2017, and the joint Ph.D. degree (cum Laude) in electrical engineering from Politecnico di Milano, and the University of Craiova, in 2023. From 2017 to 2019, he was an Assistant Researcher with the Electric Power Research Institute, China Southern Power Grid. He is currently a Postdoctoral Researcher with the Energy Department, Aalborg University. His research interests include electromagnetic interference of power converters, EMI mitigation, filter design, and experimental procedures.

ARUN D. KHILNANI (Student Member, IEEE) received the bachelor's degree in electrical engineering from the University of Mumbai, India, in 2009, and the master's degree in electric power engineering from the Chalmers University of Technology, Sweden, in 2019. He is currently pursuing the Ph.D. degree with the Department of the Electrical and Electronic Engineering, University of Nottingham. His research interests are focused on electromagnetic compatibility and power electronics.

XINGLONG WU (Member, IEEE) received the double M.Sc. degrees from Xi'an Jiaotong University, Xi'an, China, and Politecnico di Milano, Milan, Italy, in 2015, and the Ph.D. degree (summa cum laude) from Politecnico di Milano, in 2019, all in electrical engineering.

He is currently an Assistant Professor with the Department of Electronics, Information and Bioengineering, Politecnico di Milano. From March 2017 to June 2017, he was a Visiting Scientist with the Electromagnetics Group, Department of Information Technology, Ghent University, Belgium. From 2019 to 2020, he was a Postdoctoral Research Fellow with Politecnico di Milano. His research interests include distributed parameter circuit modeling, statistical techniques for electromagnetic compatibility (EMC), experimental procedures and setups for EMC testing, power electronics EMC, and system-level EMC.

Dr. Wu was a recipient of the International Union of Radio Science (URSI) Young Scientist Award from the 2020 URSI General Assembly and Scientific Symposium.

XIAOKANG LIU (Senior Member, IEEE) received the double M.Sc. degrees in electrical engineering from Xi'an Jiaotong University, Xi'an, China, and Politecnico di Milano, Milan, Italy, in 2016, and the Ph.D. degree (summa cum laude) in electrical engineering from Politecnico di Milano, in 2021.

He is currently an Assistant Professor with the Department of Electronics, Information, and Bioengineering, Politecnico di Milano. His research interests include electromagnetic compatibility, power electronics, and signal integrity. He was a recipient of the International Union of Radio Science Young Scientist Award, in 2021, and the 2021 Richard B. Schulz Best EMC Transactions Paper Award.

SERGIO A. PIGNARI (Fellow, IEEE) received the Laurea (M.Sc.) and Ph.D. degrees in electronic engineering from Politecnico di Torino, Turin, Italy, in 1988 and 1993, respectively. From 1991 to 1998, he was an Assistant Professor with the Department of Electronics, Politecnico di Torino. In 1998, he joined Politecnico di Milano, Milan, Italy, where he is currently a Full Professor of circuit theory and electromagnetic compatibility (EMC) with the Department of Electronics, Information, and Bioengineering. He was the Chair of the B.Sc. and M.Sc. study programs in electrical engineering, from 2015 to 2020. He is the author or coauthor of more than 220 papers published in international journals and conference proceedings. His research interests include EMC, field-to-wire coupling and crosstalk, conducted immunity and emissions in multi-wire structures, statistical techniques for EMC prediction, and experimental procedures and setups for EMC testing. His research activity is mainly related to aerospace, automotive, energy, and railway industry sectors.

He was a co-recipient of the 2005, 2016, and 2021 IEEE EMC Society Transactions Prize Paper Award, and the IEEE EMC Society Technical Achievement Award, in 2011. From 2010 to 2015, he served as the IEEE EMC Society Chapter Coordinator. From 2007 to 2009, he was the Chair for the IEEE Italy Section EMC Society Chapter. He served as the Italian URSI Officer for Electromagnetic Noise and Interference (Commission E), from 2015 to 2018. He has been the Technical Program Chair of the ESA Workshop on Aerospace EMC, since 2009, and a member of the Technical Program Committee of the Asia–Pacific International Symposium on EMC, since 2010. He is serving as an Associate Editor for IEEE Transactions on Electromagnetic Compatibility.

DAVID W. P. THOMAS (Senior Member, IEEE) received the B.Sc. degree in physics from Imperial College London, London, U.K., in 1981, the M.Phil. degree in space physics from The University of Sheffield, Sheffield, U.K., in 1984, and the Ph.D. degree in electrical engineering from the University of Nottingham, Nottingham, U.K., in 1990. He is a Professor of electromagnetics applications with the George Green Institute for Electromagnetics Research, University of Nottingham. His research interests include electromagnetic compatibility, electromagnetic simulation, power system transients, and power system protection. He is a member of CIGRE, several conference committees, and the EMC Europe International Steering Committee; a Convener of the Joint Working Group C4.31 EMC between communication circuits and power system; and the Chair of COST Action IC 1407 advanced characterization and classification of radiated emissions in densely integrated technologies.

MARK SUMNER (Senior Member, IEEE) received the B.Eng. degree in electrical and electronic engineering from the University of Leeds, in 1986, and the Ph.D. degree in induction motor drives from the University of Nottingham, U.K., in 1990. He was with Rolls Royce Ltd., U.K. He was also a research assistant and a lecturer, in October 1992. He is currently a Professor of electrical energy systems with the Power Electronics, Machines and Control Group, University of Nottingham. His research interests include control of power electronic systems, including sensorless motor drives, diagnostics and prognostics for drive systems, power electronics for enhanced power quality, and novel power system fault location strategies.

FLAVIA GRASSI (Senior Member, IEEE) received the Laurea (M.Sc.) and Ph.D. degrees in electrical engineering from Politecnico di Milano, Milan, Italy, in 2002 and 2006, respectively.

She is currently a Full Professor with the Department of Electronics, Information and Bioengineering, Politecnico di Milano. From 2008 to 2009, she was with the European Space Agency (ESA), ESA/ESTEC, The Netherlands, as a Research Fellow. Her research interests include theoretical and experimental characterization of EM interference via lumped and distributed circuit modeling; characterization and development of measurement procedures and setups for EMC assessment of avionic, automotive, and power systems; and statistical techniques, EMC, and coexistence issues in power systems.

Dr. Grassi received the International Union of Radio Science (URSI) Young Scientist Award, in 2008; the IEEE Young Scientist Award at the 2016 Asia–Pacific International Symposium on EMC (APEMC); the IEEE EMC Society 2016 and 2021 Transactions Prize Paper Award; and the Best Symposium Paper Award at the 2015 and 2018 APEMC.

● ● ●